Title

Real-time observation of structure and dynamics during the liquid-to-solid transition of FUS LC

Journal

Biophysical Journal, 120(7)

ISSN

0006-3495

Authors

Berkeley, Raymond F
Kashefi, Maryam
Debelouchina, Galia T

Publication Date

2021-04-01

DOI

10.1016/j.bpj.2021.02.008

Peer reviewed

Biophysical Journal
Article

Biophysical Society

Real-time observation of structure and dynamics during the liquid-to-solid transition of FUS LC

Raymond F. Berkeley,[1] Maryam Kashefi,[1] and Galia T. Debelouchina[1,*]
[1]Department of Chemistry and Biochemistry, University of California, San Diego, La Jolla, California

ABSTRACT A subset of the proteins found in pathological protein fibrils also exhibit tendencies for liquid-liquid phase separation (LLPS) both in vitro and in cells. The mechanisms underlying the connection between these phase transitions have been challenging to study due to the heterogeneous and dynamic nature of the states formed during the maturation of LLPS protein droplets into gels and solid aggregates. Here, we interrogate the liquid-to-solid transition of the low-complexity domain of the RNA-binding protein FUS (FUS LC), which has been shown to adopt LLPS, gel-like, and amyloid states. We employ magic-angle-spinning NMR spectroscopy, which has allowed us to follow these transitions in real time and with residue-specific resolution. We observe the development of β-sheet structure through the maturation process and show that the final state of FUS LC fibrils produced after LLPS is distinct from that grown from fibrillar seeds. We also apply our methodology to FUS LC G156E, a clinically relevant FUS mutant that exhibits accelerated fibrillization rates. We observe significant changes in dynamics during the transformation of the FUS LC G156E construct and begin to unravel the sequence specific contributions to this phenomenon with computational studies of the phase-separated state of FUS LC and FUS LC G156E.

SIGNIFICANCE The presence of protein aggregates in the brain is a common pathological sign of neurodegenerative disease. Recent work has revealed that a subset of the proteins found in these aggregates can also form liquid-liquid droplets and gels. Although the interconversion from one state to another can have vast implications for cell function and disease, the molecular mechanisms that underlie these processes are not well understood. Here, we combine magic-angle-spinning NMR spectroscopy with other biophysical and computational tools to follow the transitions of the RNA-binding protein FUS. This approach has allowed us to observe real-time changes in structure and dynamics as the protein undergoes these transitions, and to reveal the intricate effects of disease-relevant mutations on the transformation process.

INTRODUCTION

Neuronal protein aggregates are hallmarks of neurodegenerative disease whose biological genesis is still poorly understood (1,2). Although their cellular functions may vary, proteins found in these aggregates can contain intrinsically disordered domains with low-complexity (LC) charge-patterned sequences. These sequences not only promote the adoption of fibrillar or aggregated states but are also important drivers for liquid-liquid phase separation (LLPS) and the formation of membraneless organelles (3,4). As such, many proteins that are found in pathological neuronal aggregates can exist in different biophysical states that span a broad range of dynamic regimes, including liquid-liquid droplets, hydrogels, and amyloid fibrils. Some examples include proteins associated with Alzheimer disease (tau) (5–10), Parkinson's disease (α-synuclein) (11–14), and frontotemporal lobar degeneration (TDP-43 and FUS) (15,16).

Recent work has started to establish connections between these biophysical states in vitro. For example, the repeated coacervation and dissolution of liquid droplets of RNA-binding proteins such as hnRNPA1 has been shown to accelerate the formation of protein aggregates (17). Imaging experiments often show fibrils that grow from the center of TDP-43, FUS, and hnRNPA1 droplets, suggesting that phase-separated protein environments may serve as centers for the nucleation and growth of amyloid in the presence or absence of RNA (18–20). Reversible amyloid-like fibers of

Submitted October 19, 2020, and accepted for publication February 8, 2021.

*Correspondence: gdebelouchina@ucsd.edu

Editor: Jason Kahn.
https://doi.org/10.1016/j.bpj.2021.02.008

FUS segments have also been found embedded within hydrogels (21). Although it is known that phase separation is not a requirement for the growth of fibrils in vitro (6), the growing body of evidence linking mature LLPS protein droplets and hydrogels to aggregates and fibrils suggests that the aberrant transition between these states could be a physiologically relevant factor in disease pathogenesis (7,16,19).

The current biophysical toolbox contains well-established methodologies that can characterize each of those states separately. For example, liquid droplets have been analyzed with a variety of imaging, spectroscopic, and computational approaches that have provided valuable information regarding the sequence requirements and the nature of protein-protein interactions that drive LLPS (20,22–34). On the other hand, magic-angle-spinning (MAS) NMR spectroscopy and cryoelectron microscopy (cryo-EM) have revealed the common structural principles that underlie the formation of stable, β-sheet-rich amyloid fibrils (5,16,35–37). Although more challenging because of their viscous, dynamic, and heterogeneous nature, hydrogels have also been amenable to characterization by MAS NMR approaches (38,39). Yet, to establish a comprehensive view of how these states are connected on the molecular level and how these connections may break in disease requires a strategy that can ideally observe these transformations in real time and in the same sample at atomic resolution. Here, we explore the capability of MAS NMR spectroscopy to achieve this goal.

MAS NMR spectroscopy is a versatile structural technique that allows the investigation of biological samples of different sizes, complexity, and material state (40,41). Although the NMR resonances arising from these proteins may show line broadening because of slow molecular tumbling, strong dipolar interactions, and chemical shift anisotropy, the line broadening can be removed by spinning the sample at 54.7° (the magic angle) (42,43). During MAS, tailored pulse sequences can reintroduce the magnetic spin interactions in a controlled manner that allows the extraction of structural information such as the chemical shift, the protonation state, the distance between atoms, or their relative orientation. Spin-spin interactions can be reintroduced based on the scalar couplings between covalently bonded atoms, similar to solution NMR, enabling the description of the mobile components in the sample (44). On the other hand, dipolar-based pulse sequences can be used to identify protein regions or sample components that experience slow motions and detectable dipolar interactions through space (45). The combination of the two approaches provides the opportunity to dynamically edit the NMR spectra and to describe both the mobile and rigid components of the sample (46).

In previous work, we have used MAS NMR spectroscopy to follow the transition from the liquid droplet to the gel state of the chromatin related protein HP1α (47). This approach allowed us to detect specific serine residues that experience large changes in mobility and that appear to be important for the formation of cross-linking interactions in the gel state. Here, we extend this approach to the LC domain of the RNA-binding protein Fused in sarcoma (FUS), and we follow the transformation of individual samples of FUS LC from the liquid droplet to the gel and amyloid states in real time. We also compare the wild-type sequence and a sequence that harbors a pathogenic G156E mutation known to increase the likelihood of amyotrophic lateral sclerosis-spectrum diseases in patients (19). This mutation is particularly interesting from the biophysical point of view as it introduces additional negative charge in the sequence of FUS LC. However, unlike other FUS modifications such as phosphorylation or phosphomimetic substitutions that introduce negative charge and impede LLPS, the G156E mutation not only supports LLPS but also greatly accelerates the onset of FUS fibrils in vitro (16,19,48). To gain further insight into the molecular origins of this puzzling behavior, we complement our experimental studies with coarse-grained simulations of wild-type and G156E FUS LC and uncover subtle differences in the protein-protein interaction landscape of their liquid-droplet states. These differences may be amplified through the subsequent steps of the transformation process leading to the increased aggregation propensity of the G156E mutation.

MATERIALS AND METHODS

Expression of FUS LC and related constructs

FUS LC was prepared from recombinant Rosetta (DE3) competent *Escherichia coli* cells (MilliporeSigma, Burlington, MA) that had been transformed with a plasmid encoding the 6xHis-MBP-TEV-FUS (1–163) sequence. This plasmid was a gift from Nicolas Fawzi (RRID: Addgene_98653; Addgene plasmid no. 98653; http://n2t.net/addgene:98653, Addgene, Watertown, MA) (48). Seed cultures were grown to saturation from freshly transformed colonies and inoculated at a 1% v/v ratio into either Luria-Bertani or $^{15}N/^{13}C$-M9 medium supplemented with kanamycin (50 μg/mL). The cultures were grown at 37°C to an OD600 of ~0.7 and protein expression was induced by the addition of 1 mM isopropyl-β-D-thiogalactoside. The cultures were allowed to express protein for 4 h at 37°C before being harvested by centrifugation at 10,000 $\times$ g and 4°C for 30 min. After decanting the supernatant, cell pellets were stored at −80°C for later use. In addition to the wild-type FUS LC fusion protein, the pathogenic mutant FUS LC G156E protein was prepared. To generate the mutant, the requisite G to E mutation was introduced to the wild-type FUS LC plasmid using an NEBuilder HiFi DNA Assembly Cloning Kit (New England Biolabs, Ipswich, MA). Expression and purification conditions of the G156E mutant protein were identical to those of the wild-type.

Purification of FUS LC and related constructs

Here, we followed the published protocol by Burke et al. with some modifications (31). The frozen cell pellet was thawed, resuspended in lysis buffer (20 mM sodium phosphate, 300 mM sodium chloride, Roche cOmplete EDTA-free Protease Inhibitor Cocktail (MilliporeSigma, Burlington, MA) (pH 7.4, 4°C), and lysed by pulsed sonication for 30 min at 4°C using a Qsonica sonicator (Qsonica, Newton, CT) with a 1/8″ diameter probe tip at 12 kHz

(60%) output. The lysate was cleared by centrifugation at 20,000 × *g* for 30 min and the supernatant was incubated with Thermo Scientific HisPur Ni-NTA Resin (Thermo Fisher Scientific, Waltham, MA) for 30 min at 4°C. The suspension of beads was washed with 10 column volumes of lysis buffer containing 10 mM imidazole, and protein was eluted with two column volumes of lysis buffer containing 250 mM imidazole. The eluted protein was incubated with 6xHis-tagged Tobacco Etch Virus (TEV) protease at a ratio of 1:150 TEV to MBP-FUS LC for 5 h and 25°C to cleave MBP from FUS LC. FUS LC crashes out upon cleavage to yield a cloudy suspension with white clumps of aggregated protein. After TEV cleavage, 8 M urea was added to the reaction mixture to solubilize the aggregated FUS LC. The TEV reaction was monitored by SDS-PAGE (note that FUS LC does not bind Coomassie, so cleavage was verified by the gel shift of the MBP band). The mixture containing solubilized FUS LC was diluted to 2 mg/ml with 20 mM CAPS and 150 mM sodium chloride (pH 11), and subjected to size-exclusion chromatography over a GE HiLoad 16/600 Superdex 75-pg column (GE Healthcare, Chicago, IL). Purity was verified by high-performance liquid chromatography (HPLC), mass spectrometry, and by comparing the A260 and A280 absorbance to verify that no nucleic acid contaminants were present in the sample. This protocol generally yields 10–15 mg of FUS LC per liter of culture in both Luria-Bertani and M9 media.

Protein labeling with small molecule fluorophores

To produce Cy3-labeled FUS LC, an FUS LC fusion protein with a Cys-Ser-Gly C-terminal tag (effectively FUS LC(1–166) S164C) was generated by introducing the requisite sequence to the wild-type FUS LC plasmid using an NEBuilder HiFi DNA Assembly Cloning Kit. The 6xHis-MBP-FUS LC(1–166) S164C construct was expressed and subjected to Ni-NTA purification as described above. The eluent containing 6xHis-MBP-FUS LC (1–166) S164C was diluted to a final concentration of 20 μM with reaction buffer (20 mM sodium phosphate, 300 mM sodium chloride (pH 7.4)), and 500 μM TCEP and 80 μM Cy3-maleamide (4 M eq.; APExBIO, Houston, TX) were added. The reaction was allowed to proceed for 60 s at 25°C in the dark before quenching with excess β-mercaptoethanol (>200 M eq.). The reaction mixture was then transferred to dialysis tubing with 10 kDa molecular weight cutoff and dialyzed twice into 20 mM sodium phosphate, 300 mM sodium chloride, and 100 μM TCEP (pH 7.4) at 4°C. Once the majority of the residual Cy3 was removed by dialysis, the labeled protein was removed from the dialysis tubing and subjected to TEV cleavage and size-exclusion chromatography as described above. The labeling efficiency was ~30% as determined by analytical HPLC and mass spectrometry.

Microscopy of liquid-liquid phase-separated droplets

LLPS was induced by the dilution of 1.8 mM stock solutions of FUS LC (with 5% FUS LC(1–166) S164C-Cy3) in 20 mM CAPS, 150 mM sodium chloride (pH 11) with 20 mM sodium phosphate, and 150 mM sodium chloride (pH 7.4) at 25°C. To mitigate the risk of aggregation and to ensure quick mixing of the components, the phosphate buffer was added to the protein stock solutions. Phase separation was apparent by the sample rapidly becoming cloudy and opaque. The phase-separated protein was added to a microscope slide and allowed to incubate quiescently over the course of the imaging experiment. To prevent both the evaporation of the buffer and the mechanical perturbation of the droplets, the borders of the microscope coverslips were coated with a small amount of vacuum grease that served to raise the slide and to hermetically seal the sample.

Fluorescence recovery after photobleaching

Droplet samples were prepared as described above and imaged on an Olympus FV1000 Confocal microscope (Olympus Scientific Solutions Americas Corp., Waltham, MA). Six droplets with 5- to 10-μm diameter were subjected to photobleaching. A circular region with a diameter of one-half of the droplet diameter was bleached for each droplet. The diameter of the bleach region spanned from the center of the droplet to the droplet edge. Photobleaching was performed for 2 s using an FV3000 Hybrid Scan Unit (Olympus Scientific Solutions Americas Corp.) in Tornado Scanning mode. Fluorescence intensity was recorded within the bleached region every 2 s. Data were normalized to the pre- and postbleach fluorescence. All microscopy images were processed with Fiji/ImageJ (49,50) and data were analyzed and visualized with SciPy tools (51–54).

Thioflavin T assays

Spectra were recorded at 25°C on a Molecular Devices SpectraMax i3x Fluorometer (Molecular Devices, San Jose, CA). The excitation wavelength was 440 nm, and emission was recorded from 465 to 520 nm at a scan speed of 1 nm/s. LLPS was induced by the dilution of 1.8 mM stock solutions of FUS LC (stored in 20 mM CAPS and 150 mM sodium chloride (pH 11)) with 20 mM sodium phosphate and 150 mM sodium chloride (pH 7.4) to a final concentration of 300 μM FUS LC. A phase-separated stock solution was kept, and an aliquot was drawn at each time point for analysis. Each aliquot contained 30 μM FUS LC and 20 μM thioflavin T (ThT) diluted with 20 mM sodium phosphate and 150 mM sodium chloride (pH 7.4).

Solid-state nuclear magnetic resonance experiments

All experiments were performed using 3.2-mm thin-walled zirconia MAS rotors with 50 μL sample volume. LLPS of 30 mg ^{15}N, ^{13}C-labeled FUS LC or ^{15}N, ^{13}C-labeled FUS LC G165E was induced as described above at a concentration of 300 μM and the droplets were transferred into the rotor by gentle centrifugation at 3000 × *g* using a device built in-house. This condensed the sample into a single proteinaceous phase with final concentration of ~400 mg/ml (23 mM). This concentration was determined based on the difference between the initial A280 absorbance of the protein sample and the final absorbance of the supernatant after rotor packing. This resulted in ~20 mg of protein inside the rotor. Spectra were acquired on a 750-MHz (17.6 T) NMR spectrometer equipped with a 3.2-mm E^{free} triple resonance HCN MAS probe (Bruker Biospin, Billerica, MA). All experiments were performed at MAS frequency of 11.11 kHz. The sample was cooled with a stream of dry nitrogen gas maintained at 285 K while we estimate that the sample temperature during the MAS experiments is 10–15° higher. More details regarding the MAS NMR experimental settings are given in the Supporting materials and methods. Data were visualized and analyzed with NMRFAM-Sparky (55). The Sparky files have been deposited at https://doi.org/10.5281/zenodo.4521765.

Statistical analysis of NMR chemical shifts

Chemical shift and protein coordinate data were acquired from the Protein Data Bank (PDB) and Biological Magnetic Resonance Bank (BMRB) with PACSY Maker (56). For each amino acid in FUS LC, the PACSY database was filtered using secondary structure classifications generated by STRIDE (57) to produce a data set of chemical shifts associated with residues in PDB structures that are in either β-sheet or random coil conformations. Only chemical shifts with unambiguous assignments were considered. Because the BMRB only contains one-dimensional (1D) assignments, chemical shifts were projected into two dimensions by considering atom connectivity for each amino acid and plotting theoretical correlations using the chemical shifts for directly bonded atoms on a per-protein basis. Data were analyzed and results were visualized using

SciPy tools (51–54). Bruker NMR data were parsed with Nmrglue (58). All codes are available upon request. It should be noted that this approach is similar to that taken by PLUQ (59).

Coarse-grained molecular dynamics simulations

Molecular dynamics simulations were performed with HOOMD-blue (60) using a set of hydrophobicity-scaled pair potentials initially described by Dignon, et al. (27). This model has been shown to be effective for simulating LLPS of FUS LC and other proteins (32,48,61,62). Briefly, the model defines three interaction potentials: a potential for bonded interactions, a single potential representing short-range nonbonded interactions, and a potential representing electrostatic interactions. Bonds are represented by a harmonic potential with a bond length of 3.8 Å and a spring constant of 10 kJ/Å^2. Short range nonbonded interactions are represented by a standard Lennard-Jones potential that has been scaled to the hydrophobicity of each interaction pair. This scaled Lennard-Jones potential was utilized as implemented in the azplugins package for HOOMD-blue (63), and the hydrophobicity scaling parameters were identical to those described in Dignon, et al. (27,64). Electrostatic interactions were represented by the Yukawa potential with a Debye screening length of 1 nm and a dielectric constant of 80 to mimic an aqueous solvent containing 100 mM salt. For each simulation, 100 FUS LC or FUS LC G156E monomers were prepared in a linear configuration using mBuild (65). The coordinates of each particle in each monomer were then randomized such that each bond length was fixed at 3.8 Å and no particles overlapped. Monomers were then packed into a 50 × 50 × 50 nm simulation cell using PACKMOL (66), resulting in a protein concentration of 22 mg/mL (1.3 mM) before phase separation. Charges and masses were assigned to each particle within HOOMD-blue. Production simulations were performed on a single NVIDIA Tesla K80 GPU. Each simulation was run for a total of 1.1 μs with 10 fs timesteps using a Langevin integrator at 300 K. Simulations were analyzed and contact maps were visualized using tools from the SciPy software stack (51–54). Simulation snapshots were visualized using Ovito Pro (67). Two 300-ns replicates of each simulation were performed and analyzed to confirm that contact map results were not dependent of the initial configuration of the simulation.

RESULTS AND DISCUSSION

Liquid droplets of FUS LC undergo transition to gels and fibers at neutral pH

The full-length FUS protein can undergo a liquid-to-solid phase transition that is accelerated by the presence of a clinically relevant G156E mutation (19). We chose to work with the N-terminal LC domain comprising residues 1–163 of the protein (FUS LC) to investigate the differential behavior of FUS LC and the pathological FUS LC G156E mutant in vitro. The LC domain of FUS has been extensively studied in the LLPS state (31,32,48) and includes segments that are known to form rigid fibril cores (16,68). We prepared recombinantly purified protein (Fig. S1 and S2) mixed with 5% Cy3-labeled FUS LC and initiated phase separation under physiological pH and low-salt conditions. We observed the immediate formation of liquid-liquid phase-separated droplets that were subsequently placed in hermetically sealed microscope slides and monitored for several weeks (Fig. 1 *A*). The well-defined droplets coarsened into gel-like structures over the course of several days. As the droplets continued to age, fibrillar structures developed that appeared to protrude from the gel cores in a manner consistent with previous reports for FUS and other proteins with LC sequences capable of undergoing liquid-to-solid phase transitions (12,21). After incubation for a full month, these fibrillar structures had grown into a dense network covering the microscope slide. Two-month-old samples were also subjected to negative staining and transmission electron microscopy (TEM) in which dense clumps of fibers were also observed (Fig. S3). In contrast to wild-type FUS LC, the FUS LC G156E mutant formed fibrillar species much more rapidly, with clear fibrillar protrusions appearing after only a day of incubation (Fig. 1 *B*). Thus, the FUS LC and FUS LC G156E constructs recapitulate the transformation behavior of the full-length protein at neutral pH as described previously (19,69,70).

The maturation of FUS LC droplets was further interrogated by fluorescence recovery after photobleaching (FRAP) experiments (Fig. S4 A). Although the recovery kinetics of FUS LC droplets decreased over the course of several weeks, fluorescence recovery was not completely abrogated even after 8 weeks, suggesting that mobile components remained in the phase-separated structures even after this long period of incubation. The FUS LC G156E sample also exhibited fast recovery at the beginning (Fig. S4 B) but transitioned quickly to a fibrillar state with limited mobility.

The observation of fibrillar structures in our FUS LC and FUS LC G156E samples by microscopy prompted us to determine whether these structures have the characteristics of β-sheet-rich amyloid fibers. ThT is a switchable small molecule fluorophore that is often used as a test for the presence of amyloid (71). We initiated LLPS of FUS LC and FUS LC G156E samples and performed a binding assay with ThT (Fig. 1 *C*). Consistent with the trends observed in the microscopy experiments, FUS LC G156E formed fibers within the first 2 days and with similar kinetics to a positive control sample containing the amyloidogenic Aβ-peptide. On the other hand, ThT fluorescence of the wild-type FUS LC sample started to increase after approximately a week, whereas a negative control sample containing solubilized FUS LC in high pH CAPS buffer did not form amyloid over the course of the experiment. Although ThT fluorescence is also sensitive to the viscosity of the solvent (72) and may increase in the liquid droplet and gel environments, the changes in fluorescence intensity are consistent with the timeline of fibrillar protrusion formation in the microscopy experiments. Therefore, we interpret the increase in ThT fluorescence for the FUS LC and the FUS LC G156E samples as an indication of β-sheet amyloid formation. We also performed the experiment in the presence of 1,6-hexanediol, a small molecule known to disrupt protein droplets (Fig. S5; (73)). In this case, no ThT fluorescence was observed over the course of this experiment indicating that under our experimental conditions LLPS and amyloid formation are coupled.

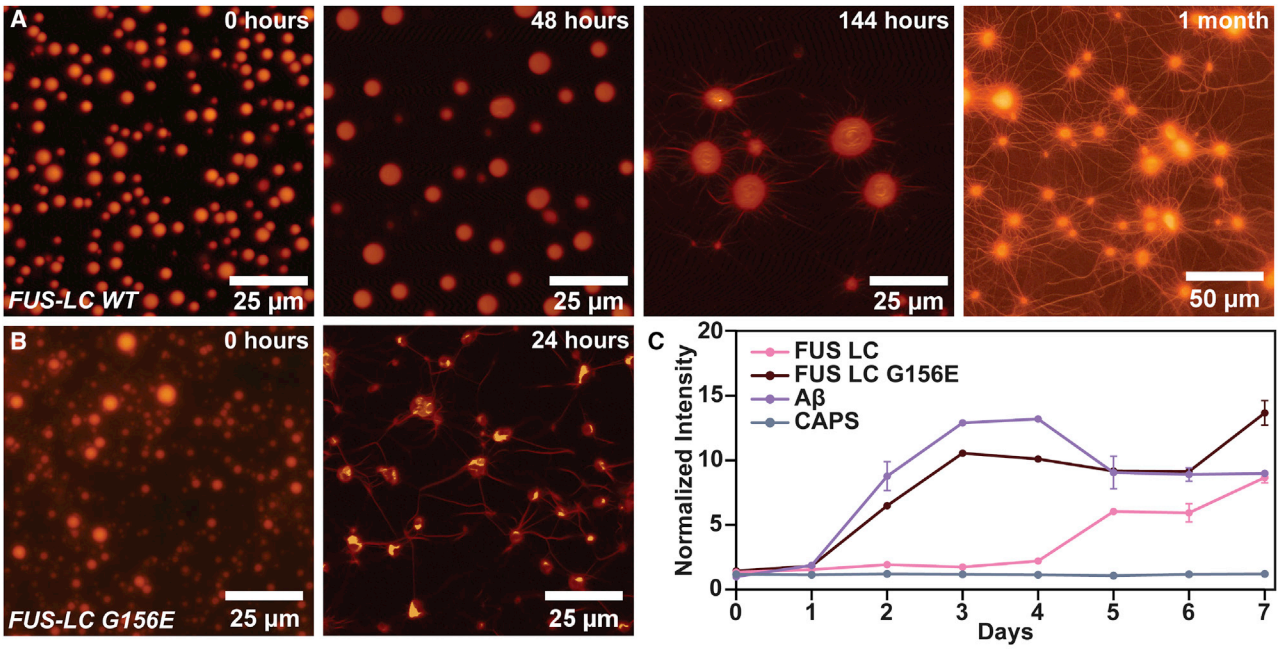

FIGURE 1 Microscopy and ThT analysis of FUS LC and FUS LC G156E maturation. (*A*) Maturation of wild-type FUS LC droplets. Droplets coarsen and loosen their spherical character after 48 h. Fibrils begin to appear after 144 h. After a full month, a dense fibril network is visible. (*B*) Maturation of FUS LC G156E droplets. The progression of the G156E mutant is accelerated, with aggregates and fibrils appearing after 24 h. (*C*) Fibrillization rates of FUS LC and FUS LC G156E characterized by ThT. The Aβ peptide was used as positive control whereas FUS LC in CAPS buffer (pH 11) served as negative control. The error bars represent standard deviation from three independent measurements.

Taken together, the imaging, FRAP, and ThT data indicate that wild-type FUS LC droplets can coarsen into gel-like states and mature into amyloid fibrils over time under near-physiological conditions. For the FUS LC G156E mutant, the transition from droplets to gels is more abrupt and the formation of the amyloid state is significantly accelerated.

The structure and dynamics of FUS LC change during the transformation process

The interactions and dynamics of FUS LC in the liquid-droplet state have been characterized extensively by solution NMR (31,32,48). On the other hand, solid-state MAS NMR spectroscopy and cryo-EM have revealed several possible amyloid states that can be formed by FUS LC (16,35,36,68). We sought to establish a connection between these observations by following the transformation from droplet to amyloid on the molecular level in real time using MAS NMR. The maturation of FUS LC droplets into gels and fibrils is ideally suited to this approach as the transformation of the wild-type protein takes several weeks and, thus, allows sufficient time for the collection of multidimensional NMR experiments at different time points.

To capture the range of dynamic regimes within the sample, we performed two different types of MAS NMR experiments. First, the INEPT-based pulse sequence was used to capture mobile components in the sample. This can include the mobile segments of an otherwise slow tumbling protein system or the mobile subpopulation of proteins in a heterogeneous sample (16,47,74,75). Second, dipolar-based experiments such as cross-polarization (CP) were used to describe the slow tumbling (rigid) components of the sample like those subpopulations in the gel and amyloid states (76,77). As control, we also used a direct polarization (DP) ^{13}C experiment which detects all carbon atoms in the sample irrespective of their mobility. We prepared two samples, one of ^{15}N,^{13}C FUS LC and one of ^{15}N,^{13}C FUS LC G156E, and subjected each to LLPS. The LLPS droplets were then gently collapsed into a single condensed phase and into an MAS NMR rotor. The final concentration of both FUS LC constructs was ~23 mM; within the range of the expected concentration of FUS LC in LLPS droplets (32). We used INEPT, CP, and DP experiments to follow the transformation of the samples over the course of 30 days for FUS LC and 12 days for FUS LC G156E (Fig. 2).

The two samples exhibited different behavior over the course of these experiments. For the wild-type FUS LC sample, the CP signal started to increase after a week, eventually reaching a plateau at 3.5 times the original integrated signal (Fig. 2, *A* and *C*). This indicates the emergence of rigid components in the sample with a timeline that is consistent with the formation of the fibrillar species detected by microscopy and ThT fluorescence. Furthermore, a comparison of the initial and final CP spectra shows the appearance of several new peaks (Fig. 2 *A*; Fig. S6, *A* and *B*). This includes peaks

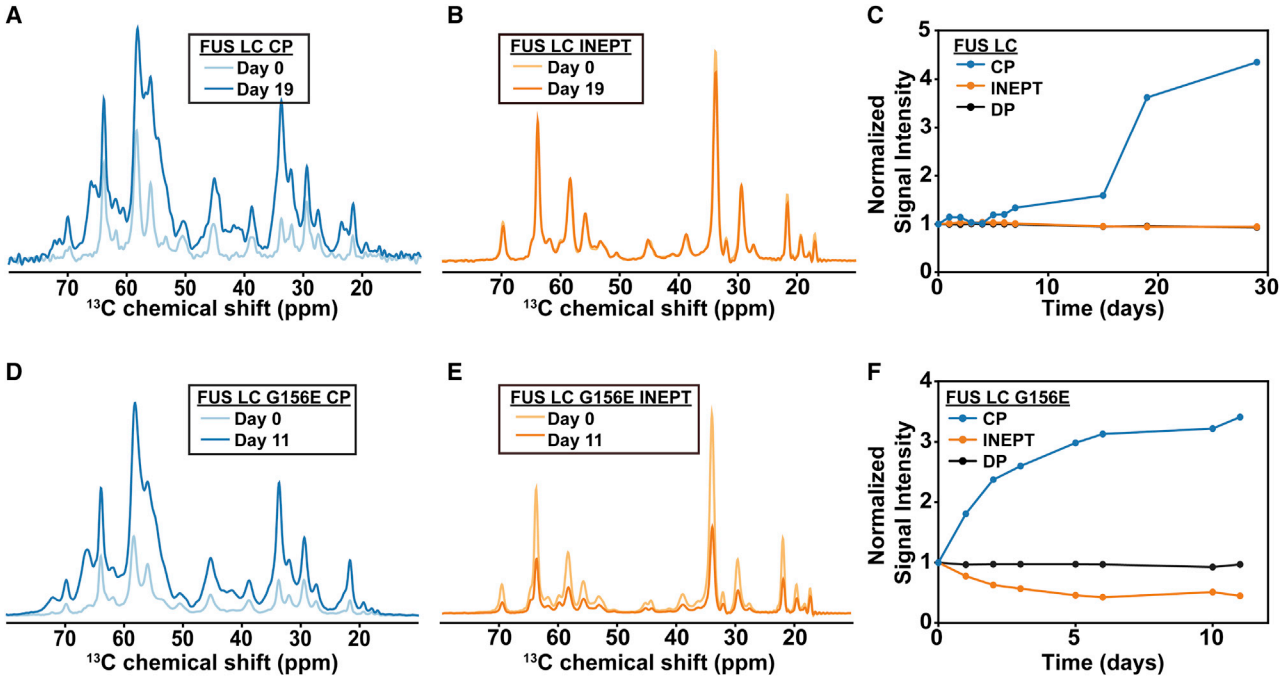

FIGURE 2 Characterization of FUS LC and FUS LC G156E maturation by MAS NMR spectroscopy. (*A*) Early and late-stage FUS LC CP spectra are shown. (*B*) Early and late-stage FUS LC INEPT spectra are shown. (*C*) Integrated signal intensity of the aliphatic region of FUS LC over time for CP, INEPT, and DP experiments is shown. (*D*) Early and late-stage FUS LC G156E CP spectra are shown. (*E*) Early and late-stage FUS LC G156E INEPT spectra are shown. (*F*) Integrated signal intensity of the aliphatic region of FUS LC G156E over time for CP, INEPT and DP experiments is shown. The error bars are based on the integrated noise level and are too small to visualize.

consistent with the chemical shifts of threonine, serine, and potentially glycine, asparagine, aspartate, and tyrosine. These peaks represent new chemical environments and suggest that the rigid components in the sample undergo a structural change over time, perhaps from an unstructured or oligomeric state to a β-sheet-rich amyloid fold. In contrast, the FUS LC G156E sample changed much more rapidly over the course of a week (Fig. 2, *D* and *F*). A comparison of the CP spectra shows a 3-fold increase in signal and the appearance of new structural environments during this time (Fig. S6, *C* and *D*). Overall, the initial and final CP spectra have similar shapes between the two samples although there are differences in intensity and line width for some peaks (Fig. S7, *A* and *C*).

The time course of the INEPT experiments is also noteworthy. Although the INEPT spectra of the wild-type protein changed very little over the course of three weeks (Fig. 2, *B* and *C*), the signals of the G156E sample decreased significantly during the first week, and then stabilized at ~50% of the initial intensity (Fig. 2, *E* and *F*). In these heterogenous samples, the INEPT signals are consistent with random coil confirmation and potentially arise from three different processes. First, they may reflect mobile monomers or low-molecular-weight oligomers that experience fast diffusion and rotational correlation times. These mobile components should also be detectable in FRAP experiments and, as our data indicate, their contribution diminishes over time (Fig. S4). Second, the INEPT signals may result from the gel phase. The gel state forms early on and involves the formation of noncovalent cross-linking interactions between monomers. These interactions may involve only certain regions of the monomer while other segments remain mobile enough to be detected by INEPT. We have observed this scenario in other protein systems that undergo gelation (47). And finally, the INEPT signals may arise from mobile regions of the amyloid state. For example, the published structure of seeded amyloid fibers of FUS LC (1–214) has a rigid β-sheet core that spans 57 residues (39–95), while the C-terminus is dynamic and unstructured and clearly visible in INEPT experiments (16). In addition, the relative ratio of gel to amyloid might determine the INEPT trajectory. For example, in the wild-type sample the buildup of β-sheet structure is slow, and the majority of the protein most likely remains in the gel state throughout the time course of the experiment. In a situation where the gel state dominates and there is a large mobile component, the INEPT signal should remain relatively constant over time, which is what we observe for the FUS LC sample. On the other hand, the G156E mutant sample quickly converts to amyloid, thus reducing the contribution of the gel state. Even if the final fibril structure contains mobile regions, the overall INEPT signal may still decrease. A final note regarding dynamics is that in heterogeneous and viscous samples such as this one, there are often motions on an intermediate timescale that are too slow for INEPT-based experiments and too fast for CP-based experiments (46). Thus,

it is possible that our experimental strategy is "blind" to some of the cross-linking interactions that contribute to the gel state or to some of the oligomeric species that lead to amyloid formation.

It should be noted that the slow transformation from a liquid-like to a more rigid β-sheet-rich state described here is distinct from the temperature dependent formation of reversible gels. Previous work has indicated that, upon cooling, FUS LC liquid condensed phases rapidly become a rigid, opaque gel, resulting in line broadening and loss of signal in the ^{1}H–^{15}N HSQC spectra acquired under solution NMR conditions (31). This reversible gel state forms quickly (within seconds), melts quickly (with seconds of heating), and is distinct from the "hydrogel" state (78), which forms by transition (rather than phase separation) of a solution of concentrated protein into amyloid fibrils. Using MAS NMR spectroscopy, we observe a similar reversible phenomenon with our initial stage FUS LC droplet samples (Fig. S8). When the sample temperature was decreased by 15°C, the ^{13}C INEPT signals almost disappeared. At the same time, the CP signals arising from rigid components increased in intensity but also in line width. The process was reversible, as an increase in temperature brought back the signals to their initial intensity and linewidth (although some small changes in the shape of the CP spectrum were noted). Similar to the solution NMR case, this behavior is consistent with the formation of reversible gels. Unlike the slow transformation described above, however, the CP signals at low temperatures did not indicate the formation of new β-sheet structures.

LLPS results in amyloid fibers with distinct structures

Intrigued by the structural changes detected in the 1D MAS NMR experiments described above, we recorded two-dimensional (2D) correlation spectra of the end-states of the two samples (30 days for FUS LC and 12 days for FUS LC G156E). In particular, we extended the 1D INEPT experiment into a 2D ^{1}H–^{13}C INEPT correlation spectrum that provides a more detailed picture of the residues that remain mobile at the end of the time course (Fig. 3 *A*). The 2D INEPT spectra of the wild-type and G156E samples contain similar amino acid types (including glycine, threonine, serine, glutamine, alanine, proline, and methionine) with chemical shifts that are consistent with random coil. The INEPT spectrum of the G156E construct has lower intensity overall despite the comparable number of scans and sample amount in the rotor, consistent with the 50% reduction of INEPT signal observed over the course of the 1D experiments. Despite the general overlap between the two spectra, a careful comparison reveals differences in the glycine region where one set of glycine residues remains the same and another set experiences a different chemical environment. This is also supported by the 1D INEPT spectra (Fig. S7, *B* and *D*) in which the G156E Gly Cα-region clearly shows two peaks. Although we were not able to assign these two different glycine groups, there appears to be subtle differences between the dynamic environments in the wild-type and mutant FUS LC samples.

To complement the residue-specific studies of mobile sample components, we also recorded 2D ^{13}C–^{13}C DARR spectra of the final state (Fig. 3 *B*). This experiment relies on a dipolar-assisted rotational resonance condition to recouple ^{13}C atoms in protein regions that experience reduced motions and rotational correlation times (79). Given the composition of the two samples, this experiment is expected to report on the rigid core of the final amyloid state. Both samples gave rise to relatively well-resolved DARR spectra where many individual crosspeaks could be identified and analyzed. To determine whether the spectra indeed report on a β-sheet-rich amyloid fold, we compared the position of the crosspeaks against a statistical analysis of chemical shifts deposited in the BMRB and the PDB (Fig. S9). Plotting these distributions with our DARR spectrum reveals that many of the correlations lie nearer to the center of the β-sheet distribution than the coil-like distribution. These observations suggest that the rigid components appearing in our DARR spectrum contain β-sheet structure.

Unlike previous studies of FUS LC fibrils (16,35,68), which used seeded fibers in isolation, our samples are a heterogeneous mixture of gel-like and fibrillar states. Therefore, the signal-to-noise in the dipolar experiments is relatively low, and this precluded the collection of other multidimensional MAS NMR correlations (e.g., three-dimensional NCACX and three-dimensional NCOCX). While this prevented us from performing site-specific assignments of the DARR spectra, we were able to compare our data with the DARR spectra of the published FUS LC (1–214) structure of seeded amyloid fibers (Fig. S10; (16)). This comparison revealed significant differences between the two spectra. First, our spectrum is relatively broader, indicating the presence of heterogeneity and/or intermediate dynamics that can interfere with the timescale of the NMR experiment and cause line broadening. This is expected as our sample is more heterogenous and dynamic by design. Second, a significant number of crosspeaks appear to be shifted or missing from our spectrum. This includes crosspeaks for the unique residues Asp46 and Pro72 that appear to be substantially shifted as well as crosspeaks for residues such as Gln93 that are not present altogether. Other residues that potentially experience different environments or are not part of the core include Thr45, Thr47, Ser70, Thr78, and Ser90.

Recent structural studies of FUS LC fibrils have indicated the presence of two possible β-sheet cores (16,68). In constructs that comprise residues 1–214 or 1–110, the β-sheet core spans residues 39–95 and has the same structure in both cases. In a construct that lacks the N-terminal portion of the sequence and covers residues 111–214, a different β-sheet core can be formed by residues

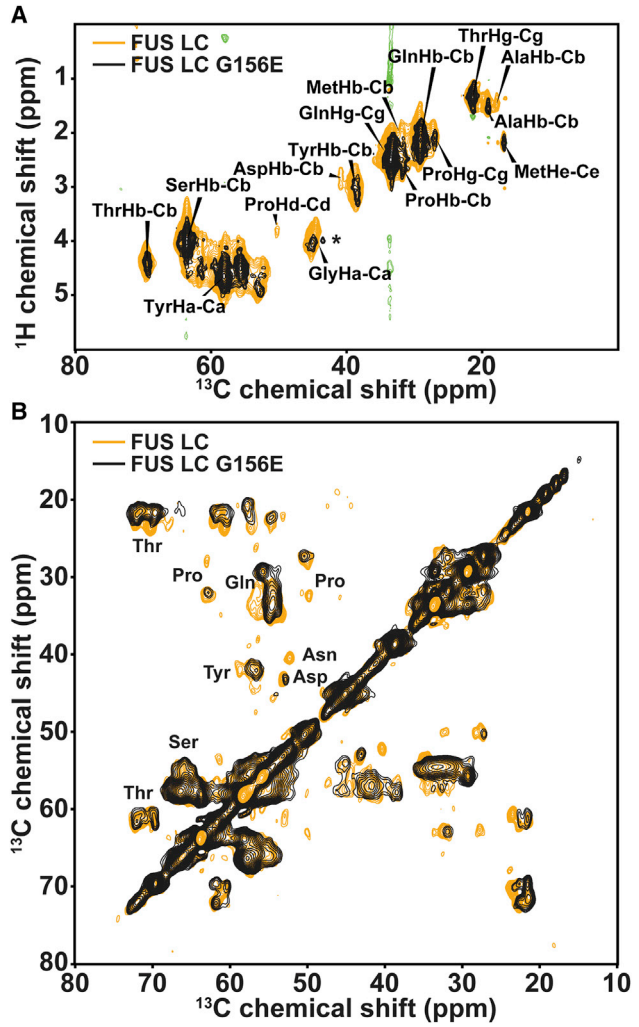

FIGURE 3 2D correlation spectra of FUS LC and FUS LC G156E. (*A*) End-state ^{1}H–^{13}C INEPT spectra of FUS LC (*orange*) and FUS LC G156E (*black*) are shown. The asterisks denotes a new glycine crosspeak that appears in the FUS LC G156E sample. (*B*) End-state ^{13}C–^{13}C DARR correlation spectra of FUS LC (*orange*) and FUS LC G156E (*black*) are shown.

112–150. Because our spectrum clearly contains aspartate and multiple threonine residues, amino acids that are only present or enriched in the N-terminal portion of the sequence, we conclude that the core of the LLPS fibrils investigated here is generally located in a similar region as the 39–95 β-sheet core. However, the structure of the core is different for the LLPS-derived fibrils as manifested by the significant chemical shift changes for some crosspeaks. The missing signals for some residues (e.g., Gln93) might also indicate that the β-sheet core of the LLPS-derived fibrils is smaller compared to the 39–95 core of the seeded FUS LC (1–214) fibers. It should also be noted that our DARR spectrum contains a much more intense tyrosine Cα-Cβ-region, potentially implying a more prominent role for these residues in the structure and dynamics of the final state.

Finally, we compared the DARR spectra of the wild-type FUS LC and the G156E mutant (Fig. 3 *B*). The two spectra are much more similar to each other than to the DARR spectrum of the seeded FUS LC (1–214) amyloids. Common features among the LLSP-derived samples include the overlapping signals for Pro72 and Asp46, the prominently missing Gln93 signal, and the overlapping shapes of the threonine and serine regions of the spectra. Therefore, it appears that the LLPS-derived fibers of FUS LC and FUS LC G156E share a similar β-sheet core located in the N-terminal segment of the protein sequence. The structure and dynamics of the two folds, however, are not completely identical, as indicated by the loss of intensity and small chemical shift changes for some crosspeaks in the G156E sample.

Therefore, the combined analyses of the INEPT and DARR spectra discussed above reveal several important observations. LLPS-derived FUS LC (1–163) amyloid fibrils have a disordered C-terminus similar to the seeded fibers of FUS LC (1–214). Similarly, the LLPS-derived fibers favor an N-terminal β-sheet core approximately centered around residues 39–95 of the protein sequence. This core, however, is potentially smaller and distinctly folded compared to the N-terminal core of fibers obtained through seeding. Therefore, the liquid droplet environment appears to influence the structure of the coupled amyloid state. The crowded conditions during LLPS may favor different types of protein-protein interactions that lead to the observed differences. For example, the valence and patterning of tyrosine residues is an important determinant of FUS LLPS (4), and amyloid formation involves the formation of steric zippers with good side-chain complementarity (16,68,80). The interactions of the tyrosine residues therefore may fine tune the exact position of the steric zippers in the FUS LC fibers. FUS is an important component of cellular stress granules which have LLPS properties and are often misregulated in amyotrophic lateral sclerosis (81,82). Thus, LLPS conditions may also influence the structure of pathogenic FUS fibers in neurodegenerative disease.

The G156E mutation exposes the amyloidogenic core of FUS LC

Previous work has shown that phosphorylation of serine and threonine residues in the FUS LC domain can inhibit LLPS (16,48). Incubation at high pH also disrupts LLPS likely because of the deprotonation and subsequent negative charge of tyrosine side chains in FUS LC under these conditions (31). It is therefore noteworthy that the disease-relevant G156E mutant, which introduces a negatively charged residue into FUS LC, can not only undergo LLPS but also exhibits faster aggregation kinetics than the wild-type. Furthermore, based on the published structures of seeded fibrils (16,68) and our MAS NMR analysis, this residue does

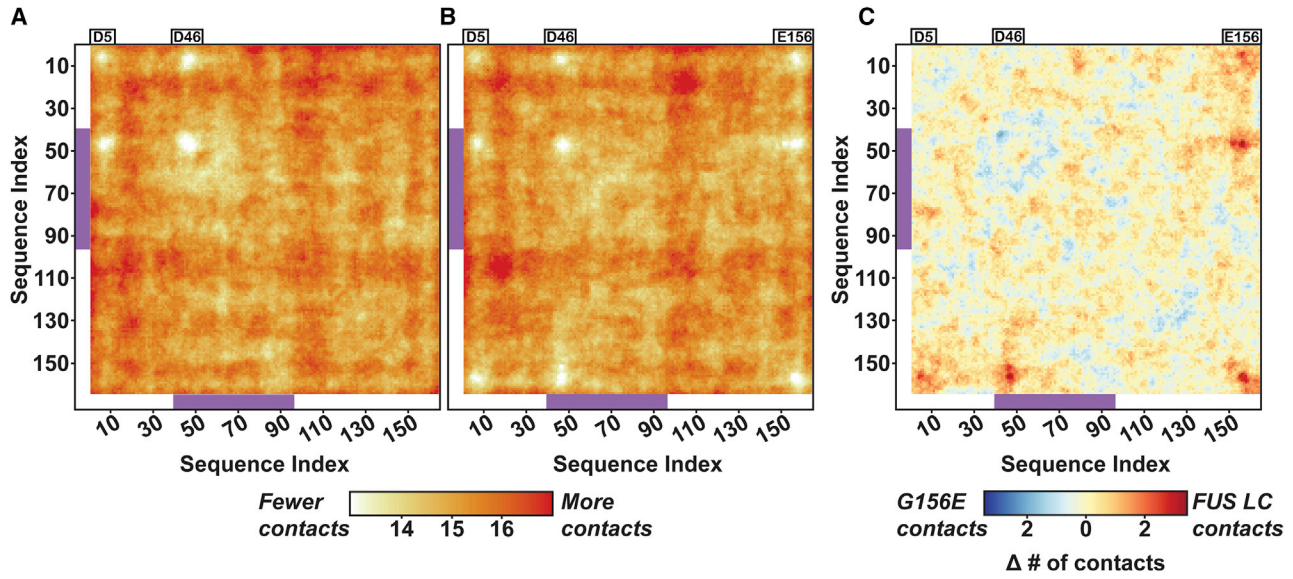

FIGURE 4 Coarse-grained simulations of FUS LC and FUS LC G156E droplets. (*A*) Intermolecular contact map for FUS LC is shown. Regions with a large number of contacts appear in orange, whereas regions with a relatively low number of contacts appear in white. (*B*) Intermolecular contact map for FUS LC G156E is shown. The color coding for both maps is the same and both maps represent contacts within a 15-Å cutoff. Distance is measured from the bead centers. (*C*) Difference map in which red indicates regions where FUS LC makes more contacts, whereas blue indicates regions where FUS LC G156E makes more contacts. The purple rectangles denote the fibril core of FUS LC (1–214) as determined in Ref. 16.

not appear to participate in the ordered fibril core. Therefore, it is still unclear how this mutation promotes amyloidogenesis from an LLPS state. To gain insight into the early events that may drive this behavior, we used coarse-grained molecular dynamics simulations to model interactions in liquid droplets formed by wild-type FUS LC and the FUS LC G156E mutant. We applied a hydrophobicity scale model (64), initially described by Dignon et al., which is capable of recapitulating LLPS in silico and has been used to analyze interactions in wild-type FUS, FUS LC, and phosphomimetic substitutions of FUS LC (27,32).

Separate simulations of 100 dispersed FUS LC or FUS LC G156E monomers in random configurations were prepared and allowed to proceed for 1.1 μs. In both simulations, dispersed monomers rapidly coalesced into a dynamic droplet-like state within 30 ns. The droplet persisted throughout the simulation (Fig. S11), with some monomers occasionally breaking free from the LLPS droplet and rejoining after a few ns. We analyzed the coalesced state by constructing intermolecular contact maps that represent the number of pair-wise amino acid contacts within a specified radius. For each simulation run, 100 frames from the droplet state were extracted and interparticle distances were measured for all particles in the simulation. Particles that were within the specified distance radius were counted as a contact. Intramolecular (i.e., intramonomer) interactions were not counted. The mean number of contacts across all frames and monomers was used to construct the contact maps.

In alignment with previous simulations of FUS LC, there are no notable regions of high contact propensity within a contact radius of up to 7 Å (Fig. S12; (32)). This is also consistent with experimental literature that suggests that LLPS of FUS LC is not driven by specific regions in the sequence (32). At longer contact distances (8–15 Å), however, some features start to appear in the contact map for FUS LC (Fig. 4 *A*; Fig. S12). This includes 1) fewer contacts between the regions surrounding the two native negatively charged residues, Asp5 and Asp46, and 2) increased contacts between a segment encompassing residues 15–25 and another segment comprising the more aliphatic region of FUS LC between residues 99–110. It is noteworthy that those interacting regions flank the rigid fibril core of the seeded fibers (39–95) but are not part of it.

The 15 Å contact map for FUS LC G156E appears similar to the contact map of the wild-type construct (Fig. 4, *B* and *C*) with one exception. The introduction of a negative charge at position 156 decreases the number of contacts between the C-terminus and the N-terminal Asp5 and Asp 46 so that two additional repulsive regions are observed in the map. Overall, the repulsion between these negatively charged residues results in reduced interactions of the C-terminus with the N-terminal part of the protein. On the other hand, the higher contact propensities of regions 15–25 and 99–110 do not appear to be affected by the presence of the additional negative charge. These conclusions hold across three different simulations with independent starting conditions for each sample and are not caused by surface effects (Fig. S13 and S14). In light of these observations, we propose that the introduction of the G156E mutation into FUS LC reduces the number of

nonproductive interactions between the termini and leads to greater exposure of the inner segments of the protein. This increases the propensity for protein-protein interactions that, in turn, leads to amyloid formation on an accelerated timescale.

CONCLUSION

The LC domain of FUS can undergo phase transitions that lead to the formation of liquid droplets, gels, and amyloid. Our work demonstrates that that FUS LC droplets formed at neutral pH mature into amyloid-like states over the course of several weeks, a transition that can be significantly accelerated by the disease-relevant mutation G156E. The slow kinetics of the process allowed us to follow this transition by MAS NMR spectroscopy and to observe the formation of characteristic β-sheet signatures at residue-specific resolution in real time. Whereas the resulting β-sheet core of these LLPS-derived fibrils is located in the same region of the sequence as the rigid core formed by seeded fibers, the core structure of the LLPS-derived fibrils appears to be different. Furthermore, when the LLPS environment was eliminated by the addition of 1,6-hexanediol, no amyloid fibrils were observed in the course of the experiment. These observations imply that liquid droplet environments can influence both the efficiency of fibril formation and their structural signatures. As FUS is often located in stress granules in the cell (81), the crowded conditions promoted by LLPS may play an important role in its pathogenic amyloid formation.

In contrast to the differences observed between the fibril core structure of seeded FUS LC fibrils and LLPS-derived fibrils, the fibril core structures of the LLPS-derived FUS LC and FUS LC G156E constructs appear relatively similar to each other. The most striking differences between the wild-type protein and the pathological mutant were maturation rate rather than the final structure, with the FUS LC G156E protein forming fibrils much earlier than its wild-type counterpart under the same conditions. Although the wild-type FUS LC sample has a significant mobile component even after several weeks, the G156E mutant matures much more rapidly and loses mobility over the course of several days. Thus, a single negatively charged mutation at a region of the sequence that does not participate in fibril core interactions can have dramatic consequences on the fibrillization process. Our coarse-grained simulations suggest that the presence of this negatively charged residue near the C-terminus increases the repulsion between the termini and promotes enhanced intermolecular contacts between inner regions of the protein. This mechanism may also explain the increased aggregation propensity of the full-length G156E mutant (19).

Our approach presented here combines imaging, MAS NMR spectroscopy, and computational methods to provide new molecular insights into the elusive transformation of a protein from the liquid droplet to the gel and amyloid states. Our strategy is versatile and provides a platform for the analysis of other proteins that exhibit similar behavior in viscous and heterogeneous environments. This approach can also be extended to explore the role of relevant biological components and small molecules on phase separation, gelation and amyloid formation.

SUPPORTING MATERIAL

Supporting Material can be found online at https://doi.org/10.1016/j.bpj.2021.02.008.

AUTHOR CONTRIBUTIONS

R.F.B. and G.T.D. conceived the project and wrote the manuscript. R.F.B. prepared samples, performed microscopy, ThT assays, NMR experiments, and computational studies. M.K. performed ThT assays and NMR experiments. G.T.D. performed NMR experiments and supervised the study. All authors analyzed the data and commented on the manuscript.

ACKNOWLEDGMENTS

We are grateful to A. de Angelis for help with the NMR spectrometers, to J. Yang's lab at UCSD for help with the ThT assays, to T. Meerloo for help with TEM, to J. Mittal for generously sharing simulations code, and to N. Fawzi for helpful discussions and comments.

This work was supported by a Research Education Component associated with NIH Grant P30 AG062429, an R21 AG069064 award to G.T.D., a T32 GM112584 fellowship to R.F.B., the BRC for NMR Molecular Imaging of Proteins at UCSD (P41 EB002031), and the UCSD Microscopy Core (NINDS NS047101).

REFERENCES

1. Soto, C., and S. Pritzkow. 2018. Protein misfolding, aggregation, and conformational strains in neurodegenerative diseases. *Nat. Neurosci.* 21:1332–1340.
2. Mathieu, C., R. V. Pappu, and J. P. Taylor. 2020. Beyond aggregation: pathological phase transitions in neurodegenerative disease. *Science.* 370:56–60.
3. Wang, J., J.-M. Choi, …, A. A. Hyman. 2018. A molecular grammar governing the driving forces for phase separation of prion-like RNA binding proteins. *Cell.* 174:688–699.e16.
4. Martin, E. W., A. S. Holehouse, …, T. Mittag. 2020. Valence and patterning of aromatic residues determine the phase behavior of prion-like domains. *Science.* 367:694–699.
5. Fitzpatrick, A. W. P., B. Falcon, …, S. H. W. Scheres. 2017. Cryo-EM structures of tau filaments from Alzheimer's disease. *Nature.* 547:185–190.
6. Lin, Y., Y. Fichou, …, S. Han. 2020. Electrostatically driven complex coacervation and amyloid aggregation of tau are independent processes with overlapping conditions. *ACS Chem. Neurosci.* 11:615–627.
7. Wegmann, S., B. Eftekharzadeh, …, B. T. Hyman. 2018. Tau protein liquid-liquid phase separation can initiate tau aggregation. *EMBO J.* 37:e98049.
8. Dregni, A. J., V. S. Mandala, …, M. Hong. 2019. In vitro 0N4R tau fibrils contain a monomorphic β-sheet core enclosed by dynamically heterogeneous fuzzy coat segments. *Proc. Natl. Acad. Sci. USA.* 116:16357–16366.

9. Ambadipudi, S., J. Biernat, …, M. Zweckstetter. 2017. Liquid-liquid phase separation of the microtubule-binding repeats of the Alzheimer-related protein Tau. *Nat. Commun.* 8:275.

10. Ambadipudi, S., J. G. Reddy, …, M. Zweckstetter. 2019. Residue-specific identification of phase separation hot spots of Alzheimer's-related protein tau. *Chem. Sci. (Camb.).* 10:6503–6507.

11. Schweighauser, M., Y. Shi, …, M. Goedert. 2020. Structures of α-synuclein filaments from multiple system atrophy. *Nature.* 585:464–469.

12. Ray, S., N. Singh, …, S. K. Maji. 2020. α-Synuclein aggregation nucleates through liquid-liquid phase separation. *Nat. Chem.* 12:705–716.

13. Araki, K., N. Yagi, …, H. Mochizuki. 2019. Parkinson's disease is a type of amyloidosis featuring accumulation of amyloid fibrils of α-synuclein. *Proc. Natl. Acad. Sci. USA.* 116:17963–17969.

14. Tuttle, M. D., G. Comellas, …, C. M. Rienstra. 2016. Solid-state NMR structure of a pathogenic fibril of full-length human α-synuclein. *Nat. Struct. Mol. Biol.* 23:409–415.

15. Li, Y. R., O. D. King, …, A. D. Gitler. 2013. Stress granules as crucibles of ALS pathogenesis. *J. Cell Biol.* 201:361–372.

16. Murray, D. T., M. Kato, …, R. Tycko. 2017. Structure of FUS protein fibrils and its relevance to self-assembly and phase separation of low-complexity domains. *Cell.* 171:615–627.e16.

17. Gui, X., F. Luo, …, D. Li. 2019. Structural basis for reversible amyloids of hnRNPA1 elucidates their role in stress granule assembly. *Nat. Commun.* 10:2006.

18. Babinchak, W. M., R. Haider, …, W. K. Surewicz. 2019. The role of liquid-liquid phase separation in aggregation of the TDP-43 low-complexity domain. *J. Biol. Chem.* 294:6306–6317.

19. Patel, A., H. O. Lee, …, S. Alberti. 2015. A liquid-to-solid phase transition of the ALS protein FUS accelerated by disease mutation. *Cell.* 162:1066–1077.

20. Lin, Y., D. S. Protter, …, R. Parker. 2015. formation and maturation of phase-separated liquid droplets by RNA-binding proteins. *Mol. Cell.* 60:208–219.

21. Liu, Z., S. Zhang, …, C. Liu. 2020. Hsp27 chaperones FUS phase separation under the modulation of stress-induced phosphorylation. *Nat. Struct. Mol. Biol.* 27:363–372.

22. Mitrea, D. M., B. Chandra, …, R. W. Kriwacki. 2018. Methods for physical characterization of phase-separated bodies and membraneless organelles. *J. Mol. Biol.* 430:4773–4805.

23. Mittag, T., and J. D. Forman-Kay. 2007. Atomic-level characterization of disordered protein ensembles. *Curr. Opin. Struct. Biol.* 17:3–14.

24. Martin, E. W., and T. Mittag. 2018. Relationship of sequence and phase separation in protein low-complexity regions. *Biochemistry.* 57:2478–2487.

25. van der Lee, R., M. Buljan, …, M. M. Babu. 2014. Classification of intrinsically disordered regions and proteins. *Chem. Rev.* 114:6589–6631.

26. Brangwynne, C. P., P. Tompa, and R. V. Pappu. 2015. Polymer physics of intracellular phase transitions. *Nat. Phys.* 11:899–904.

27. Dignon, G. L., W. Zheng, …, J. Mittal. 2018. Sequence determinants of protein phase behavior from a coarse-grained model. *PLOS Comput. Biol.* 14:e1005941.

28. Pak, C. W., M. Kosno, …, M. K. Rosen. 2016. Sequence determinants of intracellular phase separation by complex coacervation of a disordered protein. *Mol. Cell.* 63:72–85.

29. Feric, M., N. Vaidya, …, C. P. Brangwynne. 2016. Coexisting liquid phases underlie nucleolar subcompartments. *Cell.* 165:1686–1697.

30. Dignon, G. L., R. B. Best, and J. Mittal. 2020. Biomolecular phase separation: from molecular driving forces to macroscopic properties. *Annu. Rev. Phys. Chem.* 71:53–75.

31. Burke, K. A., A. M. Janke, …, N. L. Fawzi. 2015. Residue-by-Residue view of in vitro FUS granules that bind the C-terminal domain of RNA polymerase II. *Mol. Cell.* 60:231–241.

32. Murthy, A. C., G. L. Dignon, …, N. L. Fawzi. 2019. Molecular interactions underlying liquid-liquid phase separation of the FUS low-complexity domain. *Nat. Struct. Mol. Biol.* 26:637–648.

33. Molliex, A., J. Temirov, …, J. P. Taylor. 2015. Phase separation by low complexity domains promotes stress granule assembly and drives pathological fibrillization. *Cell.* 163:123–133.

34. Banani, S. F., A. M. Rice, …, M. K. Rosen. 2016. Compositional control of phase-separated cellular bodies. *Cell.* 166:651–663.

35. Murray, D. T., and R. Tycko. 2020. Side chain hydrogen-bonding interactions within amyloid-like fibrils formed by the low-complexity domain of FUS: evidence from solid state nuclear magnetic resonance spectroscopy. *Biochemistry.* 59:364–378.

36. Ding, X., F. Sun, …, S.-Z. Luo. 2020. Amyloid-forming segment induces aggregation of FUS-LC domain from phase separation modulated by site-specific phosphorylation. *J. Mol. Biol.* 432:467–483.

37. Iadanza, M. G., R. Silvers, …, S. E. Radford. 2018. The structure of a β_2-microglobulin fibril suggests a molecular basis for its amyloid polymorphism. *Nat. Commun.* 9:4517.

38. Ader, C., S. Frey, …, M. Baldus. 2010. Amyloid-like interactions within nucleoporin FG hydrogels. *Proc. Natl. Acad. Sci. USA.* 107:6281–6285.

39. Kennedy, S. B., E. R. deAzevedo, …, M. Hong. 2001. Dynamic structure of a protein hydrogel: a solid-state NMR study. *Macromolecules.* 34:8675–8685.

40. Mandala, V. S., and M. Hong. 2019. High-sensitivity protein solid-state NMR spectroscopy. *Curr. Opin. Struct. Biol.* 58:183–190.

41. Marchanka, A., B. Simon, …, T. Carlomagno. 2015. RNA structure determination by solid-state NMR spectroscopy. *Nat. Commun.* 6:7024.

42. Andrew, E. R., A. Bradbury, and R. G. Eades. 1958. Nuclear magnetic resonance spectra from a crystal rotated at high speed. *Nature.* 182:1659.

43. Maricq, M. M., and J. S. Waugh. 1979. NMR in rotating solids. *J. Chem. Phys.* 70:3300–3316.

44. Baldus, M., and B. H. Meier. 1996. Total correlation spectroscopy in the solid state. The use of scalar couplings to determine the through-bond connectivity. *J. Magn. Reson. A.* 121:65–69.

45. Takegoshi, K., S. Nakamura, and T. Terao. 2001. 13C–1H dipolar-assisted rotational resonance in magic-angle spinning NMR. *Chem. Phys. Lett.* 344:631–637.

46. Matlahov, I., and P. C. A. van der Wel. 2018. Hidden motions and motion-induced invisibility: dynamics-based spectral editing in solid-state NMR. *Methods.* 148:123–135.

47. Ackermann, B. E., and G. T. Debelouchina. 2019. Heterochromatin protein HP1α gelation dynamics revealed by solid-state NMR spectroscopy. *Angew. Chem. Int.Ed.* 58:6300–6305.

48. Monahan, Z., V. H. Ryan, …, N. L. Fawzi. 2017. Phosphorylation of the FUS low-complexity domain disrupts phase separation, aggregation, and toxicity. *EMBO J.* 36:2951–2967.

49. Schindelin, J., I. Arganda-Carreras, …, A. Cardona. 2012. Fiji: an open-source platform for biological-image analysis. *Nat. Methods.* 9:676–682.

50. Rueden, C. T., J. Schindelin, …, K. W. Eliceiri. 2017. ImageJ2: ImageJ for the next generation of scientific image data. *BMC Bioinformatics.* 18:529.

51. Virtanen, P., R. Gommers, …, P. van Mulbregt; SciPy 1.0 Contributors. 2020. SciPy 1.0: fundamental algorithms for scientific computing in Python. *Nat. Methods.* 17:261–272.

52. McKinney, W. 2010. Data structures for statistical computing in Python. *Proceedings of the 9th Python in Science Conference.* 445:56–61.

53. Hunter, J. D. 2007. Matplotlib: a 2D graphics environment. *Comput. Sci. Eng.* 9:90–95.

54. Harris, C. R., K. J. Millman, …, T. E. Oliphant. 2020. Array programming with NumPy. *Nature.* 585:357–362.

55. Lee, W., W. M. Westler, …, J. L. Markley. 2009. PINE-SPARKY: graphical interface for evaluating automated probabilistic peak assignments in protein NMR spectroscopy. *Bioinformatics.* 25:2085–2087.

56. Lee, W., W. Yu, …, J. L. Markley. 2012. PACSY, a relational database management system for protein structure and chemical shift analysis. *J. Biomol. NMR.* 54:169–179.

57. Heinig, M., and D. Frishman. 2004. STRIDE: a web server for secondary structure assignment from known atomic coordinates of proteins. *Nucleic Acids Res.* 32 (*Suppl 2*):W500–W502.

58. Helmus, J. J., and C. P. Jaroniec. 2013. Nmrglue: an open source Python package for the analysis of multidimensional NMR data. *J. Biomol. NMR.* 55:355–367.

59. Fritzsching, K. J., Y. Yang, …, M. Hong. 2013. Practical use of chemical shift databases for protein solid-state NMR: 2D chemical shift maps and amino-acid assignment with secondary-structure information. *J. Biomol. NMR.* 56:155–167.

60. Anderson, J. A., J. Glaser, and S. C. Glotzer. 2020. HOOMD-blue: a Python package for high-performance molecular dynamics and hard particle Monte Carlo simulations. *Comput. Mater. Sci.* 173:109363.

61. Schuster, B. S., G. L. Dignon, …, J. Mittal. 2020. Identifying sequence perturbations to an intrinsically disordered protein that determine its phase-separation behavior. *Proc. Natl. Acad. Sci. USA.* 117:11421–11431.

62. Conicella, A. E., G. L. Dignon, …, N. L. Fawzi. 2020. TDP-43 α-helical structure tunes liquid-liquid phase separation and function. *Proc. Natl. Acad. Sci. USA.* 117:5883–5894.

63. mphowardlab/azplugins, 2020. mphowardlab.

64. Kapcha, L. H., and P. J. Rossky. 2014. A simple atomic-level hydrophobicity scale reveals protein interfacial structure. *J. Mol. Biol.* 426:484–498.

65. Klein, C., J. Sallai, …, P. T. Cummings. 2016. A hierarchical, component based approach to screening properties of soft matter. *In* Foundations of Molecular Modeling and Simulation: Select Papers from FOMMS 2015. R. Q. Snurr, C. S. Adjiman, D. A. Kofke, R. Q. Snurr, C. S. Adjiman, and D. A. Kofke, eds, pp. 79–92.

66. Martínez, L., R. Andrade, …, J. M. Martínez. 2009. PACKMOL: a package for building initial configurations for molecular dynamics simulations. *J. Comput. Chem.* 30:2157–2164.

67. Stukowski, A. 2009. Visualization and analysis of atomistic simulation data with OVITO–the Open Visualization Tool. *Model. Simul. Mater. Sci. Eng.* 18:015012.

68. Lee, M., U. Ghosh, …, R. Tycko. 2020. Molecular structure and interactions within amyloid-like fibrils formed by a low-complexity protein sequence from FUS. *Nat. Commun.* 11:5735.

69. Murakami, T., S. Qamar, …, P. St George-Hyslop. 2015. ALS/FTD mutation-induced phase transition of FUS liquid droplets and reversible hydrogels into irreversible hydrogels impairs RNP granule function. *Neuron.* 88:678–690.

70. Nomura, T., S. Watanabe, …, Y. Furukawa. 2014. Intranuclear aggregation of mutant FUS/TLS as a molecular pathomechanism of amyotrophic lateral sclerosis. *J. Biol. Chem.* 289:1192–1202.

71. Naiki, H., K. Higuchi, …, T. Takeda. 1989. Fluorometric determination of amyloid fibrils in vitro using the fluorescent dye, thioflavin T1. *Anal. Biochem.* 177:244–249.

72. Stsiapura, V. I., A. A. Maskevich, …, K. K. Turoverov. 2008. Thioflavin T as a molecular rotor: fluorescent properties of thioflavin T in solvents with different viscosity. *J. Phys. Chem. B.* 112:15893–15902.

73. Kroschwald, S., S. Maharana, and A. Simon. 2017. Hexanediol: a chemical probe to investigate the material properties of membraneless compartments. *Matters (Zur.).* 3:e201702000010.

74. Andronesi, O. C., S. Becker, …, M. Baldus. 2005. Determination of membrane protein structure and dynamics by magic-angle-spinning solid-state NMR spectroscopy. *J. Am. Chem. Soc.* 127:12965–12974.

75. Debelouchina, G. T., G. W. Platt, …, R. G. Griffin. 2010. Magic angle spinning NMR analysis of β2-microglobulin amyloid fibrils in two distinct morphologies. *J. Am. Chem. Soc.* 132:10414–10423.

76. Hartmann, S. R., and E. L. Hahn. 1962. Nuclear double resonance in the rotating frame. *Phys. Rev.* 128:2042–2053.

77. Pines, A., M. G. Gibby, and J. S. Waugh. 1972. Proton-enhanced nuclear induction spectroscopy. A method for high resolution NMR of dilute spins in solids. *J. Chem. Phys.* 56:1776–1777.

78. Kato, M., T. W. Han, …, S. L. McKnight. 2012. Cell-free formation of RNA granules: low complexity sequence domains form dynamic fibers within hydrogels. *Cell.* 149:753–767.

79. Takegoshi, K., S. Nakamura, and T. Terao. 2003. 13C–1H dipolar-driven 13C–13C recoupling without 13C rf irradiation in nuclear magnetic resonance of rotating solids. *J. Chem. Phys.* 118:2325–2341.

80. Sawaya, M. R., S. Sambashivan, …, D. Eisenberg. 2007. Atomic structures of amyloid cross-beta spines reveal varied steric zippers. *Nature.* 447:453–457.

81. Wheeler, J. R., T. Matheny, …, R. Parker. 2016. Distinct stages in stress granule assembly and disassembly. *eLife.* 5:e18413.

82. Wolozin, B., and P. Ivanov. 2019. Stress granules and neurodegeneration. *Nat. Rev. Neurosci.* 20:649–666.